



Three-dimensional morphology of equatorial plasma bubbles deduced from measurements onboard CHAMP

J. Park^{1,*}, H. Lühr¹, and M. Noja²

¹GFZ, German Research Center for Geosciences, Potsdam, Germany

²Tomtom Telematics, Berlin, Germany

* now at: Korea Astronomy and Space Science Institute, Daejeon, South Korea

Correspondence to: J. Park (pj@kasi.re.kr)

Received: 3 November 2014 – Revised: 23 December 2014 – Accepted: 5 January 2015 – Published: 28 January 2015

Abstract. Total electron content (TEC) between Low-Earth-Orbit (LEO) satellites and the Global Navigation Satellite System (GNSS) satellites can be used to constrain the three-dimensional morphology of equatorial plasma bubbles (EPBs). In this study we investigate TEC measured onboard the Challenging Minisatellite Payload (CHAMP) from 2001 to 2005. We only use TEC data obtained when CHAMP passed through EPBs: that is, when in situ plasma density measurements at CHAMP altitude also show EPB signatures. The observed TEC gradient along the CHAMP track is strongest when the corresponding GNSS satellite is located equatorward and westward of CHAMP with elevation angles of about 40–60°. These elevation and azimuth angles are in agreement with the angles expected from the morphology of the plasma depletion shell proposed by Kil et al. (2009).

Keywords. Ionosphere (ionospheric irregularities)

1 Introduction

Equatorial plasma bubbles (EPBs) are a well-known phenomenon in the low-latitude nighttime ionospheric F region. This phenomenon is characterized by precipitous depletion of plasma density. EPBs manifest themselves as backscatter plumes in range–time–intensity plots of coherent scatter radars (e.g. Hysell and Woodman, 1997), airglow depletions in the 630.0 nm all-sky camera images (e.g. Kim et al., 2002; Chapagain et al., 2012), and scintillations in electromagnetic waves from the Global Navigation Satellite System (GNSS) satellites (e.g. Straus et al., 2003; Nishioka et al., 2011). EPBs can reach altitudes of about 2000 km (e.g. Kelley et al., 2003; Mendillo et al., 2005), and their latitudinal extent can

be $\pm 20^\circ$ from the equator around solar maxima (e.g. Kelley et al., 2003, Fig. 1).

When projected on the horizontal plane, EPBs are known to exhibit inverted-C structures if they are observed from above: i.e. more poleward parts of an EPB are located further westward (e.g. Kelley et al., 2003). On the vertical plane aligned with the dip equator, EPBs manifest themselves as structures whose higher-altitude part is located further westward (e.g. Zalesak et al., 1982; Hysell et al., 2009; Hei et al., 2014). By combining these two facts (i.e. inverted-C on the horizontal plane and westward tilt on the equatorial/vertical plane) and the field-aligned nature of EPBs (e.g. Sultan, 1996), Kil et al. (2009) suggested that the three-dimensional (3-D) morphology of EPBs has a shell-like structure. According to their model: (1) the highest-altitude point of the shell structure is located westward/equatorward of any other points on the shell, and (2) shell cross-sections perpendicular to the ambient B field exhibit elongation towards westward/outward (outward = toward higher L shell) or eastward/inward directions. Park et al. (2009) supported this suggestion using the anisotropic perturbation of the magnetic field around EPBs. As ambient ionospheric currents make a detour along EPB surfaces (due to low conductivity inside EPBs), the resultant current loops are expected to generate magnetic field deflections in space pointing along the EPB surface. In Park et al. (2009) the average magnetic field deflection in the plane perpendicular to the ambient B field exhibits elongation towards a westward/outward or eastward/inward direction, which is as expected from the morphology of the plasma depletion shell proposed by Kil et al. (2009). The 3-D shell structure was also demonstrated

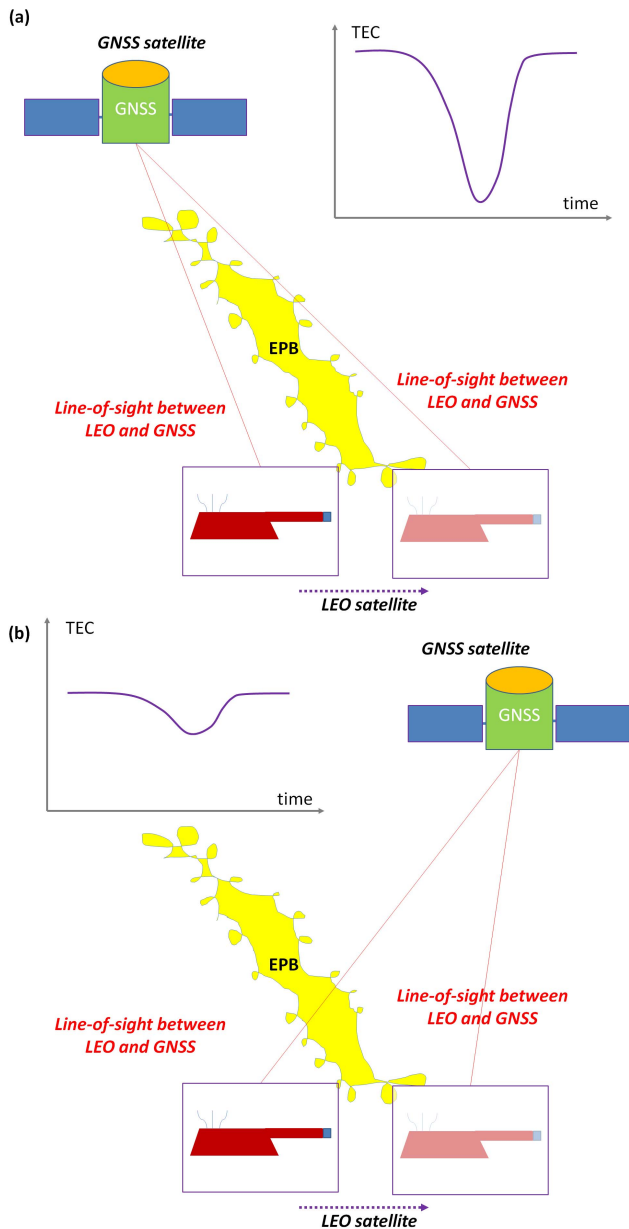


Figure 1. Schematic illustrations of the relationship between TEC fluctuation level and LOS direction between LEO and GNSS satellites: (a) the LOS and the EPB surfaces are nearly parallel, and (b) they are nearly perpendicular.

in first-principle simulations by Huba et al. (2009) and Retterer (2010).

As we have seen in the preceding paragraph, the shell structure proposed by Kil et al. (2009) can explain a number of observational properties of EPBs, such as anisotropic plume structures in coherent scatter radar data, projected inverted-C structures on the horizontal plane, and directional preferences of magnetic field deflections. Up to now, however, no observation could decisively verify the shell struc-

ture, mainly due to the lack of 3-D observation capability. This is why we need more observational evidence for the shell structure.

Low-Earth-orbit (LEO) satellites often carry dual-frequency GNSS receivers. From the LEO-GNSS communication data in dual frequencies, we can deduce total electron content (TEC), which is defined as plasma density integrated along the line-of-sight (LOS) between the LEO and GNSS satellites. These LEO-TEC data have been a useful building block in ionospheric studies (e.g. Mannucci et al., 2005; Jakowski et al., 2007). However, only a few studies (e.g. Noja et al., 2013) made use of LEO-TEC data for plasma irregularity detection in the ionosphere. Traditional plasma density probes, such as Langmuir Probes or ion traps, can only provide scalar values of plasma density. Although LEO-TEC data also give (integrated) plasma density, they can provide one more important information, the LOS direction. Making use of this directional information, we can impose further constraints on EPB geometry. For example, LEO-TEC data may answer the following question: as a LEO satellite passes through an EPB, which LOS direction sees the strongest TEC fluctuation (i.e. eastward, westward, poleward, or equatorward)? This question is schematically illustrated in the cartoons of Fig. 1. Note that LEO satellites move much faster than GNSS satellites. From Fig. 1 we expect that the TEC gradient along the LEO-satellite track should be largest when the LOS and the EPB surfaces are nearly parallel (Fig. 1a). When LOS and EPB are nearly perpendicular (Fig. 1b), small TEC gradients are expected. Therefore, if observed TEC gradient exhibits certain anisotropy (or directional preference) around EPBs, the LOS corresponding to the maximum TEC gradient can give a hint about the 3-D structure of EPBs. In the following sections we pursue the answer to these questions.

2 Instruments and data processing methods

Challenging Minisatellite Payload (CHAMP) was launched in July 2000 into a near-circular polar orbit, whose inclination angle is $\sim 87.3^\circ$, and the altitude was about 450 km right after launch. A planar Langmuir probe (PLP) onboard CHAMP measured plasma density every 15 s. A dual-frequency GNSS receiver conducted GNSS observations every 10 s, from which we can estimate TEC between CHAMP and GNSS satellites. No TEC is estimated when the elevation angle of a GNSS satellite is smaller than 24° . In this study we focus on the period from 2001 to 2005, when EPB activity was higher than during later years of the CHAMP mission (e.g. Xiong et al., 2010).

Figure 2 illustrates our data processing method. From top to bottom the panels present: (a) vertical TEC, (b) magnetic latitude (MLAT) of CHAMP, (c) elevation angle of the GNSS satellite as seen from CHAMP, (d) azimuth angle of the GNSS satellite as seen from CHAMP (counted

from geomagnetic north, positive westward), (e) TEC fluctuation level, (f) plasma density measured by the CHAMP/PLP, and (g) plasma density fluctuation level. The “vertical” TEC in panel a is calculated by multiplying slant TEC (between CHAMP and the GNSS satellite) with the mapping function given by Eq. (9) of Noja et al. (2013). The TEC fluctuation level (panel e) is defined as 3-point moving standard deviation of the vertical TEC after linear detrending. The mapping function and linear detrending are used to mitigate the influence of elevation angle on the TEC standard deviation. The plasma density fluctuation level (panel g) is calculated by subtracting large-scale variations, which are estimated by a Savitzky–Golay filter, from the CHAMP/PLP data and taking the absolute magnitude. The cutoff length scale of this high-pass filter is about 350 km, which is a compromise between the scale length used by Stolle et al. (2006) (230 km) and that of Xiong et al. (2010) (550 km). In the bottom panel the blue horizontal dashed line represents our EPB threshold ($30\,000\text{ cm}^{-3}$), which is also a compromise between the upper ($50\,000\text{ cm}^{-3}$) and lower ($20\,000\text{ cm}^{-3}$) thresholds used by Xiong et al. (2010). When the plasma density fluctuation level exceeds this threshold, CHAMP is deemed to encounter an EPB. Then, all the TEC data points within $\pm 60\text{ s}$ (marked by black squares in panel e) are bin-averaged according to the elevation angle (panel c) and azimuth angle (panel d). The bins are rectangular in a cylindrical coordinate system whose azimuth and radius represent the GNSS azimuth and co-elevation angles ($= 90^\circ$ -elevation angle), respectively. The bin size is 2° by 2° in the cylindrical coordinate system.

3 Statistical results

Polar plots in Fig. 3 show TEC fluctuation levels as a function of (co-)elevation and azimuth angles of GNSS satellites as seen from CHAMP. We have used nighttime CHAMP observations from 2001 to 2005 for Fig. 3. Note that only the TEC values obtained near in situ EPB encounters (judged by the CHAMP/PLP data fluctuations as shown in Fig. 2) are used. Figure 3a–c represent from top to bottom low-latitude Northern Hemisphere (between $+5$ and $+25^\circ\text{ N}$), equatorial region (between -10 and $+10^\circ\text{ N}$), and low-latitude Southern Hemisphere (between -25 and -5° N), respectively. In each frame the distribution of TEC fluctuation level is given versus the azimuth and co-elevation angles of GNSS satellites. The co-elevation angle of GNSS satellites is represented by radius from the origin. Concentric circles are overplotted every 20° in co-elevation angles: i.e. the centre point represents 90° in elevation angle, and the inner-most (outer-most) concentric circle represents 70° (10°) in elevation angle. The positive (negative) Y direction is towards the north (south). The colour represents bin-averaged TEC fluctuation level. Note that a two-dimensional 5-by-5 median filter has been applied to obtain Fig. 3.

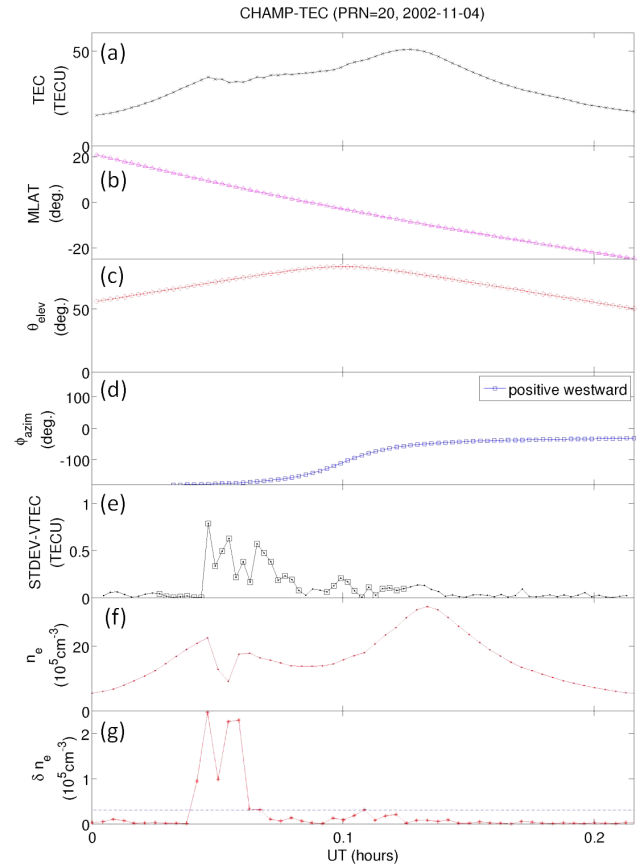


Figure 2. Illustrations of our data processing method: (a) TEC data, (b) magnetic latitude (MLAT) of CHAMP, (c) elevation angle of the GNSS satellite as seen from CHAMP, (d) azimuth angle of the GNSS satellite as seen from CHAMP (counted from geomagnetic north, positive angles are westward), (e) TEC fluctuation level, (f) plasma density measured by the CHAMP/PLP and (g) plasma density fluctuation level.

From Fig. 3a and c we can see that the TEC fluctuation level is strongest when the GNSS satellites are equatorward and westward of CHAMP. From Fig. 3b (equatorial region) TEC fluctuation level is lower than in Fig. 3a and c (low-latitude regions). Nevertheless, Fig. 3b also shows that the TEC fluctuation level is strongest when GNSS satellites are located westward of CHAMP. The elevation angle corresponding to maximum TEC fluctuation level is approximately 40 – 60° . In Fig. 3 the azimuth angles corresponding to the maximum TEC fluctuation levels are within 0 – 90° in the Southern Hemisphere and within 90 – 180° in the Northern Hemisphere.

4 Discussion

In this section we will check whether the anisotropy of TEC fluctuation level (Fig. 3) can be explained by the 3-D shell structure of EPBs proposed by Kil et al. (2009). Both upleg

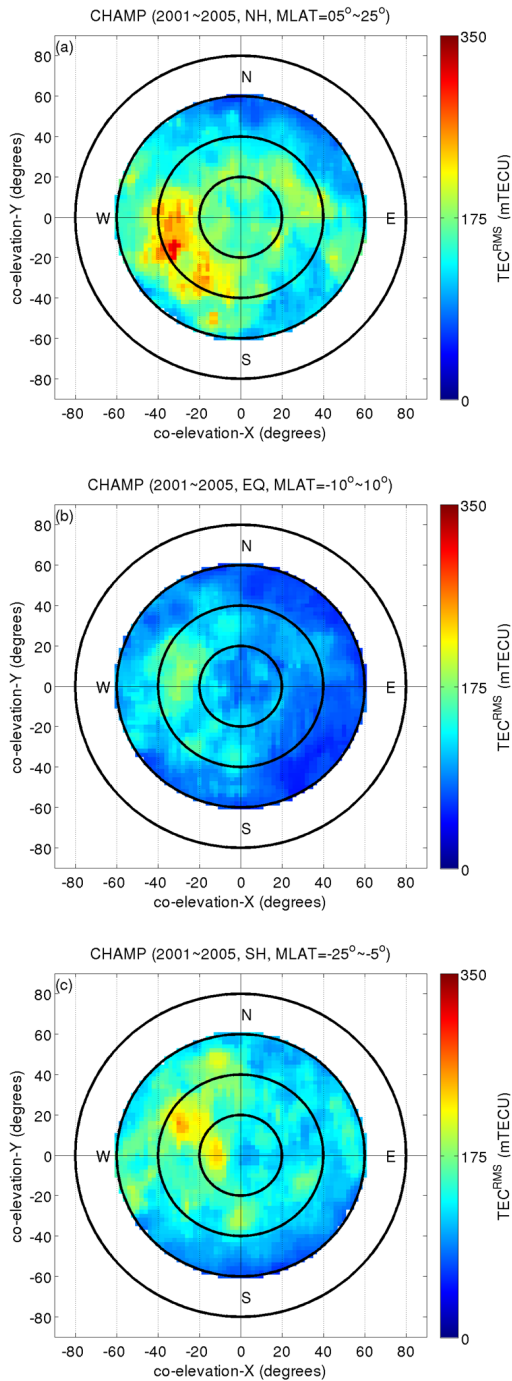


Figure 3. Polar plots showing TEC fluctuation level as a function of co-elevation and azimuth angles of GNSS satellites as seen from CHAMP: **(a)** northern low-latitude region (between $+5$ and $+25^\circ$ N), **(b)** equatorial region (between -10 and $+10^\circ$ N) and **(c)** southern low-latitude region (between -25 and -5° N). Note that only the TEC values are used which were obtained near in situ EPB encounters (judged by the CHAMP/PLP data fluctuation as shown in Fig. 2).

(CHAMP flying northbound) and downleg (southbound) data are intermingled within each frame of Fig. 3. Therefore, the patterns in Fig. 3 cannot reflect multipath noise of instrument origin, which is fixed in the spacecraft coordinate system. As alluded to in the Introduction, the TEC fluctuation level is expected to be higher when LOS between CHAMP and GNSS satellites is parallel to EPB surfaces than when it is perpendicular.

Figure 4 is a schematic illustration of an EPB shell structure, which is a bird-eye's view seen from the northeast toward the equator. The EPB shell structure originally suggested by Kil et al. (2009) has curved surfaces. However, Kil et al. (2009, Fig. 1d) and Kelley et al. (2003, Fig. 1) seem to suggest that the curvature of the shell structure is not so large. Supported by this fact, we approximate the northern surface of the EPB shell structure with a quasi-flat triangle, as shown in Fig. 4.

In Fig. 4a we expect maximum TEC fluctuation levels when the LOS passes through the apex point of the EPB shell structure (i.e. the highest-altitude point of the EPB shell). The reason is as follows. As already seen in Fig. 1, TEC fluctuation level becomes higher as the LOS becomes more parallel (or tangent) to EPB surfaces. When CHAMP is within an EPB we may draw, however, an infinite number of tangent lines to the EPB surface: e.g. both Fig. 4a and b satisfy the tangent condition although their GNSS satellite locations are different from each other. Among all these tangent LOS directions, the one containing the longest path inside the EPB should see the deepest TEC depletion, which naturally leads to largest along-track gradient of CHAMP/TEC. Although a tangent LOS with very low elevation angle (Fig. 4b) may have the longest path inside the EPB surface, no CHAMP/TEC data are used from elevation angles below 24° . Considering this elevation angle limit, the longest path inside the EPB surface is expected for the tangent LOS passing through the apex point of the EPB shell (Fig. 4a). Hence, TEC fluctuation levels measured along the LEO satellite track are expected to maximize for this specific tangent LOS (passing through the apex point of the EPB shell). The elevation and azimuth angle of this specific tangent LOS (orange arrow in Fig. 4a) can be calculated in terms of the apex height of the shell structure, structure tilt angle on the equatorial plane, and the LEO satellite latitude/altitude near the EPB encounter. First, the zonal extent of the shell structure ($a + b$ in Fig. 4a) can be expressed as

$$a + b = \frac{h_{\text{EPB}}^{\text{apex}} - h_{\text{LEO}}}{\tan\theta_{\text{tilt}}}, \quad (1)$$

where $h_{\text{EPB}}^{\text{apex}}$ is the apex height of the shell structure (i.e. the highest altitude the shell can reach at the dip equator), h_{LEO} is the altitude of the LEO satellite (CHAMP) and θ_{tilt} is the average westward tilt angle of the EPB structure within the equatorial (vertical) plane. Then, the deflection angle of the inverted-C structure within the horizontal plane ($\alpha_{\text{inverted-C}}$) can be expressed as

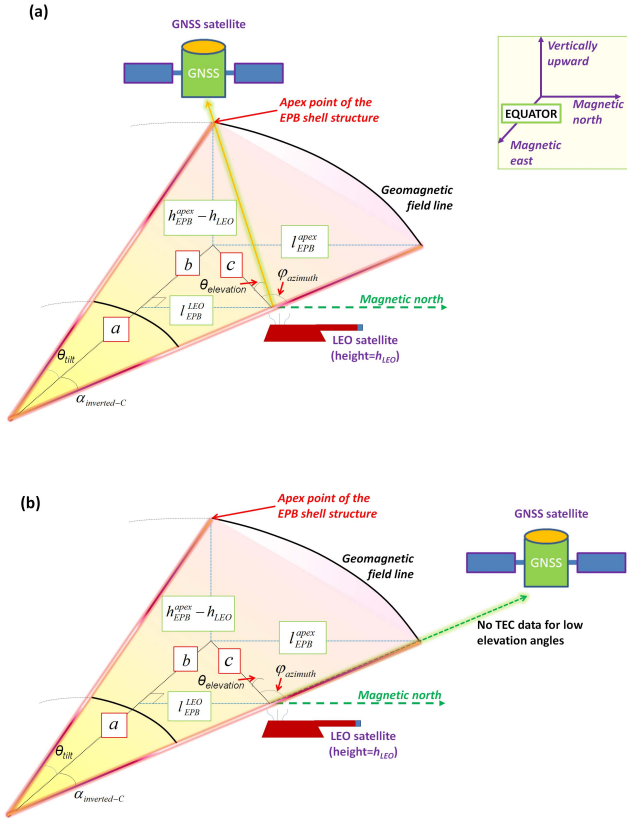


Figure 4. Schematic illustration of the EPB shell structure, in a bird-eye’s view seen from northeast toward the equator: **(a)** the elevation angle of the GNSS satellite is large, and the LOS between LEO and GNSS satellites passes through the apex point of the EPB shell structure, and **(b)** the elevation angle of the GNSS satellite is small, and the LOS between LEO and GNSS satellites is nearly horizontal and along the inverted-C signature.

$$\alpha_{\text{inverted-C}} = \tan^{-1} \left(\frac{l_{\text{EPB}}^{\text{apex}}}{h_{\text{EPB}}^{\text{apex}} - h_{\text{LEO}}} \times \tan \theta_{\text{tilt}} \right), \quad (2)$$

where $l_{\text{EPB}}^{\text{apex}}$ corresponds to the field-aligned mapping of the EPB shell apex onto the LEO satellite altitude (h_{LEO}). $l_{\text{EPB}}^{\text{apex}}$ can also be considered as the longest horizontal distance between the shell and the dip equator at the LEO satellite altitude (h_{LEO}). We assume that the LEO satellite encounters an EPB at a latitudinal position of $l_{\text{EPB}}^{\text{LEO}}$. Then, the dimensions, a , b , and c in Fig. 4a can be estimated by

$$a = \frac{l_{\text{EPB}}^{\text{LEO}}}{\tan \alpha_{\text{inverted-C}}} = \frac{l_{\text{EPB}}^{\text{LEO}}}{\frac{l_{\text{EPB}}^{\text{apex}}}{h_{\text{EPB}}^{\text{apex}} - h_{\text{LEO}}} \times \tan \theta_{\text{tilt}}} \quad (3)$$

$$= \frac{l_{\text{EPB}}^{\text{LEO}} (h_{\text{EPB}}^{\text{apex}} - h_{\text{LEO}})}{l_{\text{EPB}}^{\text{apex}} \times \tan \theta_{\text{tilt}}},$$

$$b = (a + b) - a = \frac{h_{\text{EPB}}^{\text{apex}} - h_{\text{LEO}}}{\tan \theta_{\text{tilt}}} - \frac{l_{\text{EPB}}^{\text{LEO}} (h_{\text{EPB}}^{\text{apex}} - h_{\text{LEO}})}{l_{\text{EPB}}^{\text{apex}} \times \tan \theta_{\text{tilt}}} \quad (4)$$

$$= \frac{h_{\text{EPB}}^{\text{apex}} - h_{\text{LEO}}}{\tan \theta_{\text{tilt}}} \left(1 - \frac{l_{\text{EPB}}^{\text{LEO}}}{l_{\text{EPB}}^{\text{apex}}} \right),$$

$$c = \sqrt{b^2 + (l_{\text{EPB}}^{\text{LEO}})^2} \quad (5)$$

$$= \sqrt{\left(\frac{h_{\text{EPB}}^{\text{apex}} - h_{\text{LEO}}}{\tan \theta_{\text{tilt}}} \right)^2 \left(1 - \frac{l_{\text{EPB}}^{\text{LEO}}}{l_{\text{EPB}}^{\text{apex}}} \right)^2 + (l_{\text{EPB}}^{\text{LEO}})^2},$$

Finally, the elevation ($\theta_{\text{elevation}}$) and azimuth (ϕ_{azimuth}) angle of the LOS penetrating through the shell structure apex are

$$\theta_{\text{elevation}} = \tan^{-1} \left(\frac{h_{\text{EPB}}^{\text{apex}} - h_{\text{LEO}}}{c} \right) \quad (6)$$

$$= \tan^{-1} \left(\frac{h_{\text{EPB}}^{\text{apex}} - h_{\text{LEO}}}{\sqrt{\left(\frac{h_{\text{EPB}}^{\text{apex}} - h_{\text{LEO}}}{\tan \theta_{\text{tilt}}} \right)^2 \left(1 - \frac{l_{\text{EPB}}^{\text{LEO}}}{l_{\text{EPB}}^{\text{apex}}} \right)^2 + (l_{\text{EPB}}^{\text{LEO}})^2}} \right),$$

$$\phi_{\text{azimuth}} = \pi - \tan^{-1} \left(\frac{b}{l_{\text{EPB}}^{\text{LEO}}} \right) \quad (7)$$

$$= \pi - \tan^{-1} \left(\frac{\frac{h_{\text{EPB}}^{\text{apex}} - h_{\text{LEO}}}{\tan \theta_{\text{tilt}}} \left(1 - \frac{l_{\text{EPB}}^{\text{LEO}}}{l_{\text{EPB}}^{\text{apex}}} \right)}{l_{\text{EPB}}^{\text{LEO}}} \right)$$

$$= \pi - \tan^{-1} \left(\frac{h_{\text{EPB}}^{\text{apex}} - h_{\text{LEO}}}{\tan \theta_{\text{tilt}}} \left(\frac{1}{l_{\text{EPB}}^{\text{LEO}}} - \frac{1}{l_{\text{EPB}}^{\text{apex}}} \right) \right),$$

Note that $l_{\text{EPB}}^{\text{apex}}$ and $h_{\text{EPB}}^{\text{apex}}$ in the equations are not independent because they represent magnetically conjugate points. If R_E is the Earth’s radius and β is magnetic latitude at the LEO satellite altitude, the two parameters are related as follows (e.g. Lühr and Xiong, 2010; Xiong and Lühr, 2013, Eq. 3):

$$h_{\text{EPB}}^{\text{apex}} = \frac{R_E + h_{\text{LEO}}}{\cos^2 \beta} - R_E = \frac{R_E + h_{\text{LEO}}}{1 - \sin^2 \beta} - R_E \quad (8)$$

$$\approx \frac{R_E + h_{\text{LEO}}}{1 - \left(\frac{l_{\text{EPB}}^{\text{apex}}}{R_E + h_{\text{LEO}}} \right)^2} - R_E$$

$$= \frac{(R_E + h_{\text{LEO}})^3}{(R_E + h_{\text{LEO}})^2 - (l_{\text{EPB}}^{\text{apex}})^2} - R_E,$$

Hence, the elevation ($\theta_{\text{elevation}}$) and azimuth (ϕ_{azimuth}) angles in Eqs. (6)–(7) are functions of only four independent parameters: the apex height of the shell structure ($h_{\text{EPB}}^{\text{apex}}$), the shell’s tilt angle within the equatorial plane (θ_{tilt}), and the

LEO satellite altitude (h_{LEO}) and latitude ($l_{\text{EPB}}^{\text{LEO}}$) around the EPB encounter.

By assuming reasonable values for the four independent variables, we can estimate the elevation and azimuth angles for the maximum TEC fluctuation level. The apex height of the EPB shell structure ($h_{\text{EPB}}^{\text{apex}}$) is assumed to be 2000 km, as Mendillo et al. (2005) stated that this value can be easily attained by EPBs. The latitudinal position of maximum EPB occurrence at CHAMP altitude ($h_{\text{EPB}}^{\text{LEO}} \approx 400$ km) is about 10° (about 1000 km from the equator) (Xiong et al., 2010, Fig. 9). Also, the westward tilt angle of the shell structure within the equatorial (vertical) plane is assumed to be 50° (Park et al., 2009, Fig. 4). From these assumed values, we can calculate the elevation and azimuth angles of GNSS satellites when the LOS passes through the apex point of the EPB shell structure. The resultant elevation and azimuth angles are $+50$ and $+138^\circ$ (from geomagnetic north, positive westward), respectively. This pair of values, calculated with representative values of EPB parameters, corresponds approximately to the regions of strong TEC fluctuation shown in Fig. 3a.

This calculation result does not sensitively depend on the four assumed parameters related to the EPB properties: i.e. the apex height of the shell structure ($h_{\text{EPB}}^{\text{apex}}$), the shell's tilt angle within the equatorial plane (θ_{tilt}), and LEO satellite altitude (h_{LEO}) and latitude ($l_{\text{EPB}}^{\text{LEO}}$) at the EPB encounter. We have calculated the elevation and azimuth angles for all possible combinations of the four independent parameters over a wide range: $h_{\text{EPB}}^{\text{apex}}$ (500–3000 km, every 500 km), θ_{tilt} (30 – 60° , every 10°), h_{LEO} (300–500 km, every 10 km), and $l_{\text{EPB}}^{\text{LEO}}$ (50 km– $l_{\text{EPB}}^{\text{apex}}$, every 10 km). Note that $l_{\text{EPB}}^{\text{LEO}} \leq l_{\text{EPB}}^{\text{apex}}$ because we only use the CHAMP data near EPB encounters. The mean and standard deviation of the resultant elevation angles are $40 \pm 11^\circ$. The mean and standard deviation of the resultant azimuth angles are $147 \pm 28^\circ$. These calculation results are in qualitative agreement with the observed angles for the maximum TEC fluctuation in Fig. 3 (elevation angle is approximately 40 – 60° ; approximate centre azimuth angle is 130°).

5 Summary and conclusion

From TEC and plasma density observations onboard CHAMP from 2001 to 2005, we have investigated the dependence of the TEC fluctuation level on azimuth and elevation angles of GNSS satellites as seen from CHAMP. We have only used TEC data points obtained when the in situ plasma density at CHAMP altitude exhibits EPB signatures. Our main conclusions can be summarized by the following points:

1. When CHAMP passes through EPBs, the largest TEC fluctuations are observed when LOS points to the westward/equatorward direction: at azimuth angles of 90 –

180° (0 – 90°) from geomagnetic north in the Northern (Southern) Hemisphere.

2. When CHAMP passes through EPBs, largest TEC fluctuations occur for elevation angles around 40 – 60° .
3. The anisotropic distributions of TEC fluctuations (in terms of the elevation and azimuth angles) uniquely confirm the 3-D shell structure of EPBs suggested by Kil et al. (2009).

Acknowledgements. The authors gratefully acknowledge valuable discussions with C. Xiong. The CHAMP mission was sponsored by the Space Agency of the German Aerospace Centre (DLR) through funds of the Federal Ministry of Economics and Technology, following a decision of the German Federal Parliament (grant code 50EE0944). J. Park was partially supported by the “Planetary system research for space exploration” project, the basic research funding from KASI, and the Air Force Research Laboratory, under agreement number FA2386-14-1-4004.

The service charges for this open access publication have been covered by a Research Centre of the Helmholtz Association.

Topical Editor H. Kil thanks two anonymous referees for their help in evaluating this paper.

References

- Chapagain, N. P., Taylor, M. J., Makela, J. J., and Duly, T. M.: Equatorial plasma bubble zonal velocity using 630.0 nm airglow observations and plasma drift modeling over Ascension Island, *J. Geophys. Res.*, 117, A06316, doi:10.1029/2012JA017750, 2012.
- Hei, M. A., Bernhardt, P. A., Siefing, C. L., Wilkens, M. R., Huba, J. D., Krall, J. F., Valladares, C. E., Heelis, R. A., Hairston, M. R., Coley, W. R., Chau, J. L., and De La Jara, C.: Radio-tomographic images of postmidnight equatorial plasma depletions, *Geophys. Res. Lett.*, 41, 13–19, doi:10.1002/2013GL056112, 2014.
- Huba, J. D., Ossakow, S. L., Joyce, G., Krall, J., and England, S. L.: Three-dimensional equatorial spread F modeling: Zonal neutral wind effects, *Geophys. Res. Lett.*, 36, L19106, doi:10.1029/2009GL040284, 2009.
- Hysell, D. L. and Woodman, R. F.: Imaging coherent backscatter radar observations of topside equatorial spread F, *Radio Sci.*, 32, 2309–2320, doi:10.1029/97RS01802, 1997.
- Hysell, D. L., Hedden, R. B., Chau, J. L., Galindo, F. R., Roddy, P. A., and Pfaff, R. F.: Comparing F region ionospheric irregularity observations from C/NOFS and Jicamarca, *Geophys. Res. Lett.*, 36, L00C01, doi:10.1029/2009GL038983, 2009.
- Jakowski, N., Wilken, V., and Mayer, C.: Space weather monitoring by GPS measurements on board CHAMP, *Space Weather*, 5, S08006, doi:10.1029/2006SW000271, 2007.
- Kelley, M. C., Makela, J. J., Paxton, L. J., Kamalabadi, F., Comberiate, J. M., and Kil, H.: The first coordinated ground- and space-based optical observations of equatorial plasma bubbles, *Geophys. Res. Lett.*, 30, 1766, doi:10.1029/2003GL017301, 2003.

- Kil, H., Heelis, R. A., Paxton, L. J., and Oh, S.-J.: Formation of a plasma depletion shell in the equatorial ionosphere, *J. Geophys. Res.*, 114, A11302, doi:10.1029/2009JA014369, 2009.
- Kim, Y. H., Hong, S. S., and Weinberg, J. L.: Equatorial spread F found in 5577 Å and 6300 Å airglow observations from Hawaii, *J. Geophys. Res.*, 107, 1264, doi:10.1029/2001JA009232, 2002.
- Lühr, H. and Xiong, C.: IRI-2007 model overestimates electron density during the 23/24 solar minimum, *Geophys. Res. Lett.*, 37, L23101, doi:10.1029/2010GL045430, 2010.
- Mannucci, A. J., Tsurutani, B. T., Iijima, B. A., Komjathy, A., Saito, A., Gonzalez, W. D., Guarnieri, F. L., Kozyra, J. U., and Skoug, R.: Dayside global ionospheric response to the major interplanetary events of 29–30 October 2003 “Halloween Storms”, *Geophys. Res. Lett.*, 32, L12S02, doi:10.1029/2004GL021467, 2005.
- Mendillo, M., Zesta, E., Shodhan, S., Sultan, P. J., Doe, R., Sahai, Y., and Baumgardner, J.: Observations and modeling of the coupled latitude-altitude patterns of equatorial plasma depletions, *J. Geophys. Res.*, 110, A09303, doi:10.1029/2005JA011157, 2005.
- Nishioka, M., Basu, Su., Basu, S., Valladares, C. E., Sheehan, R. E., Roddy, P. A., and Groves, K. M.: C/NOFS satellite observations of equatorial ionospheric plasma structures supported by multiple ground-based diagnostics in October 2008, *J. Geophys. Res.*, 116, A10323, doi:10.1029/2011JA016446, 2011.
- Noja, M., Stolle, C., Park, J., and Lühr, H.: Long-term analysis of ionospheric polar patches based on CHAMP TEC data, *Radio Sci.*, 48, 289–301, doi:10.1002/rds.20033, 2013.
- Park, J., Lühr, H., Stolle, C., Rother, M., Min, K. W., and Michaelis, I.: The characteristics of field-aligned currents associated with equatorial plasma bubbles as observed by the CHAMP satellite, *Ann. Geophys.*, 27, 2685–2697, doi:10.5194/angeo-27-2685-2009, 2009.
- Retterer, J. M.: Forecasting low-latitude radio scintillation with 3-D ionospheric plume models: 1. Plume model, *J. Geophys. Res.*, 115, A03306, doi:10.1029/2008JA013839, 2010.
- Stolle, C., Lühr, H., Rother, M., and Balasis, G.: Magnetic signatures of equatorial spread F as observed by the CHAMP satellite, *J. Geophys. Res.*, 111, A02304, doi:10.1029/2005JA011184, 2006.
- Straus, P. R., Anderson, P. C., and Danaher, J. E.: GPS occultation sensor observations of ionospheric scintillation, *Geophys. Res. Lett.*, 30, 1436, doi:10.1029/2002GL016503, 2003.
- Sultan, P. J.: Linear theory and modeling of the Rayleigh-Taylor instability leading to the occurrence of equatorial spread F, *J. Geophys. Res.*, 101, 26875–26891, doi:10.1029/96JA00682, 1996.
- Xiong, C. and Lühr, H.: Nonmigrating tidal signatures in the magnitude and the inter-hemispheric asymmetry of the equatorial ionization anomaly, *Ann. Geophys.*, 31, 1115–1130, doi:10.5194/angeo-31-1115-2013, 2013.
- Xiong, C., Park, J., Lühr, H., Stolle, C., and Ma, S. Y.: Comparing plasma bubble occurrence rates at CHAMP and GRACE altitudes during high and low solar activity, *Ann. Geophys.*, 28, 1647–1658, doi:10.5194/angeo-28-1647-2010, 2010.
- Zalesak, S. T., Ossakow, S. L., and Chaturvedi, P. K.: Nonlinear equatorial spread F: The effect of neutral winds and background Pedersen conductivity, *J. Geophys. Res.*, 87, 151–166, doi:10.1029/JA087iA01p00151, 1982.